Funded by
the European Union

Preprint submitted to Fractal & Fractional

A Multi-spectral Fractal Image Model and its Associated Fractal Dimension Estimator

Mihai Ivanovici

MIV Imaging and Vision Laboratory
Electronics and Computers Department
Transilvania University of Braşov, România

Abstract

We propose both a probabilistic fractal model and fractal dimension estimator for multi-spectral images. The model is based on the widely-known fractional Brownian motion fractal model, extended to the case of images with multiple spectral bands. The model is validated mathematically, under the assumption of statistically independence of the spectral components. Using this model, we generated several synthetic multi-spectral fractal images of varying complexity, with 7 statistically-independent spectral bands at specific wavelengths in the visible domain. The fractal dimension estimator is based on the widely-used probabilistic box-counting classical approach extended to the multivariate domain of multi-spectral images. We validated the estimator on the previously-generated synthetic multi-spectral images having fractal properties. Furthermore, we deployed the proposed multi-spectral fractal image estimator for the complexity assessment of real remotely-sensed data sets and showed the usefulness of the proposed approach.

keywords: fractal dimension, box counting, multi-spectral fractal images, remotely-sensed multi-spectral images

1 Introduction

Fractal geometry proposed by B. Mandelbrot in [37] triggered the computer-based analysis of self-similar and scale-independent objects called fractals and enabled its application in many domains. The fundamental fractal measure

is the fractal dimension, defined to assess the roughness or the complexity of such objects. To be more specific, the fractal dimension objectively quantifies the variations of a fractal object, or a signal exhibiting fractal properties, along the analysis scales [42]. The resulting fractal dimension is a scalar comprised in the interval $[E, E+1]$, where E is the topological dimension of a scalar-value object. For a grey-scale image, the fractal dimension is comprised between 2 and 3, taking into account that the topological dimension of the image support is $E = 2$. For an RGB color image, the color fractal dimension should belong to the interval $[E, E+3]$, that is being comprised between 2 and 5 according to [18]. By generalization, for multidimensional signals and in particular for multi-spectral images, the fractal dimension should be comprised between $[E, E+M]$, where M is the number of image spectral bands [22]. The fractal dimension has been used in a plethora of applications for the classification of signals or patterns exhibiting fractal properties, like texture images [6], [33] or for image segmentation [20] [52]. In the fields of remote sensing and Earth Observation, the fractal analysis was used for noise characterization in SAR sea-ice images [45], while the fractal dimension was used to correct scale [53].

The theoretical fractal dimension is the Hausdorff dimension [17], which cannot be used in practice due to its definition for continuous objects. Consequently, various estimators were proposed in order to allow the fractal analysis for digital images with fractal properties: the similarity dimension [37], the probability measure [51], [29], the Minkowski–Bouligand dimension, also known as Minkowski dimension or box-counting dimension [14], the δ-parallel body method also known as covering-blanket approach, morphological covers or Minkowski sausage [39], the gliding box-counting algorithm based on the box-counting approach [4], the fuzzy logic-based approaches [5], [41], the pyramidal decomposition-based approach [3]. There exist also various surveys on fractal estimators, like [25] and [47], as well as an attempt to unify several existing approaches into a single one [31]. However, all these approaches were designed for binary and grey-scale images and they are usually used without calibration or referencing to fractal images with known fractal dimension.

Various attempts were made to extend the fractal dimension estimation approaches to the multivariate image domain, starting with color and going up to the multi-spectral. The initial approaches for defining fractal measures for color images were marginal, considering each color channel independently [38]. The probabilistic box-counting approach was extended for the complexity assessment of color fractal images with independent color components and its validity was proved first mathematically and then experimentally in [18]. Some limitations of this latter approach were underlined in [19]. In [55] the

authors propose an approach based on the box counting paradigm, by dividing the image in non-overlapping blocks and considering the pixel counting in the RGB color domain, for both synthetic and natural images. In [40] extensions of the differential box counting approach were proposed for RGB color images, without a mathematical proof or a calibration. The approach proposed in [21] allows for an extension to the multi-spectral image domain. Recently, the fractal generation and fractal dimension estimation were extended to the multi-spectral image case [22], without a mathematical proof of validity of the multi-spectral fractal image model.

The domain of multi-spectral and hyper-spectral imaging, which greatly developed recently, requires the adaptation of existing tools of even the definition of new tools for image analysis. Multi-spectral and hyper-spectral imaging allows for capturing higher-resolution spectral information for a scene, covering sometimes both the visible and the infrared wavelength spectra. A better spectral resolution can provide a deeper understanding of the materials and surfaces in the scene, in particular about the land cover objects in an Earth Observation scenario [27]. Spectral imaging in a wider sense is used in a wide variety of applications, such as agriculture [49][44], forest management [43][16], geology [12][2] etc.

In this article we embrace the approach in [22], we describe it extensively, we mathematically prove the conjecture in [22] and add more experimental results both on synthetic and real multi-spectral images. More specifically, in Section 2, we propose first the extension of the mid-point displacement generation technique to the case of multi-spectral images with 7 spectral bands; secondly we visualize the generated images using three different techniques and then we prove mathematically the validity of the fractal model for the generated synthetic multi-spectral fractal bands with statistically-independent bands; in the end, we extend to the domain of multi-spectral images the probabilistic box-counting approach for the estimation of the fractal dimension. In Section 3 we tune the proposed approach on the generated synthetic multi-spectral images with 7 statistically-independent spectral bands, in the attempt of reaching the theoretical fractal dimension of the respective images. In Section 4 we estimate the fractal dimension of a real satellite image and in Section 5 we draw the conclusions.

2 Proposed approach

2.1 Theoretical considerations

From [42], the fractal dimension of a gray-scale fractal image is:

$$D = E + 1 - H = 3 - H \tag{1}$$

where $E = 2$ is the topological dimension of the image support and H is the Hurst coefficient which controls the complexity of the fractal object. The Hurst coefficient takes values between 0 and 1, a small value indicating a complex object and a great value indicating a less complex object.

From [18], it is obvious that for color fractal images with independent color components, the color fractal dimension is:

$$D_{col} = E + |RGB| - 3H = 5 - 3H \tag{2}$$

where $|RGB| = 3$ is the cardinal of the set of color channels and H is the Hurst coefficient of each color plane, assuming that the color fractal image is comprised of three color planes of the same complexity, thus the same value of the Hurst coefficient.

Equation (2) offers a less complex alternative for the estimation of color fractal dimension, based on the estimation of the Hurst parameter on the gray-scale image representing the first principal component after computing PCA on the color image data.

For the case of multi-spectral images with statistically-independent bands, the theoretical fractal dimension should be:

$$D_{MSI} = E + M - MH \tag{3}$$

where M is the number of bands. For a multi-spectral fractal image with $E = 2$ and $M = 7$ spectral bands (a septa-spectral image), like in the experimental results presented in this paper, the theoretical fractal dimension is:

$$D_{7SI} = 9 - 7H \tag{4}$$

Consequently, in theory, the highest complexity of a multi-spectral image with 7 spectral bands should be 9.

2.2 Fractal model extension to multi-spectral domain

Considering the conclusion in [18], one can extend the proposed approach for generation of color fractal images to the domain of multi-spectral and, perhaps, even hyper-spectral fractal images. Consequently, in this paper we embraced the midpoint displacement algorithm for generating fractal images based on the fractional Brownian motion model. We generated 3 multi-spectral images of different complexity: low complexity ($H = 0.9$), mid

complexity ($H = 0.5$) and high complexity ($H = 0.1$). For each of the 3 complexities, we generated 7 statistically-independent fractal images using the midpoint displacement approach [42], each of them corresponding to a wavelength or band in the resulting synthetic multi-spectral image. For the three synthetic fractal multi-spectral images, we chose the following 7 wavelengths for the corresponding spectral bands: 450, 500, 550, 600, 650 and 700 nm, all of them in the visible spectrum. The choice of the wavelengths was completely arbitrary and was done solely for visualization purposes. In Figures 1, 2 and 3, from (a) to (g) we depict the 7 spectral bands ($b_1, b_2 \cdots b_7$) of each of the three generated multi-spectral images. The random seeds used in the generation process were the same for the three multi-spectral images in order to generate similar terrain for the corresponding bands.

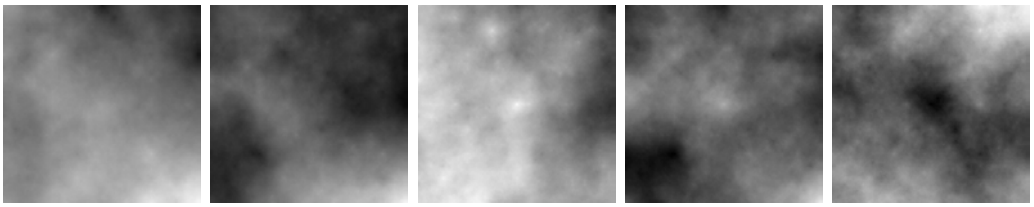

(a) b_1 (b) b_2 (c) b_3 (d) b_4 (e) b_5

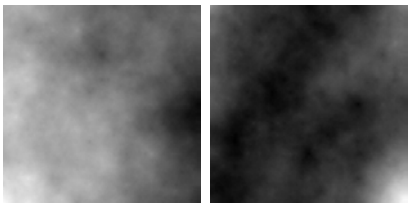

(f) b_6 (g) b_7

Figure 1: The 7 spectral bands of the MSI with low complexity ($H = 0.9$).

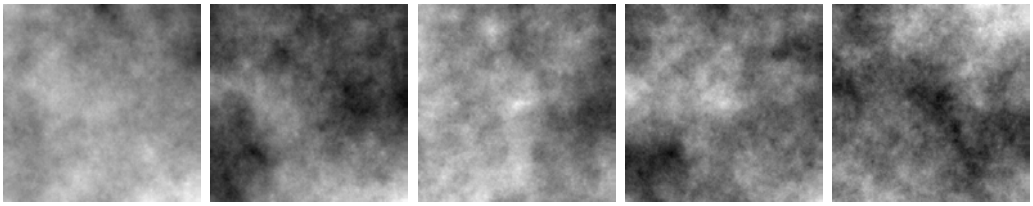

(a) b_1 (b) b_2 (c) b_3 (d) b_4 (e) b_5

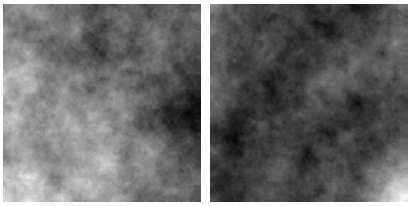

(f) b_6 (g) b_7

Figure 2: The 7 spectral bands of the MSI with medium complexity ($H = 0.5$).

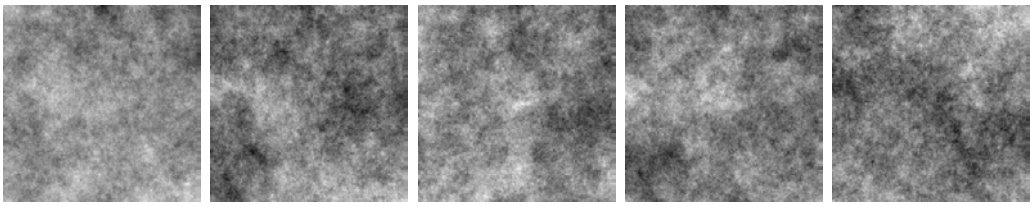

(a) b_1 (b) b_1 (c) b_1 (d) b_1 (e) b_1

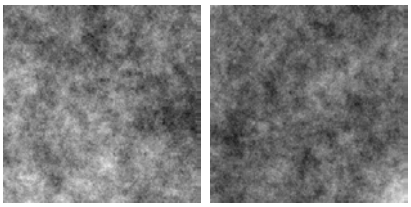

(f) b_1 (g) b_1

Figure 3: The 7 spectral bands of the MSI with high complexity ($H = 0.1$).

Next step is to assign each band in the generated multi-spectral fractal images to a certain wavelength in the visible spectrum. We arbitrarily chose the following mapping between the 7 bands of each multi-spectral fractal image (Table 1) in order to produce the actual data cubes corresponding to the synthetic multi-spectral fractal images and furthermore to be able to visualize the multi-spectral images as color RGB composite images.

b_1	b_2	b_3	b_4	b_5	b_6	b_7
$400nm$	$450nm$	$500nm$	$550nm$	$600nm$	$650nm$	$700nm$

Table 1: The arbitrary mapping between the 7 generated bands and the corresponding wavelengths.

In Figure 4 we show the resulting data cubes for the three generated multi-spectral fractal images with 7 spectral bands. Note that the pseudo coloring of each spectral band channel is used to illustrate the approximate position of the corresponding wavelength on the lambda axis, does not necessarily represent the actual color corresponding to the exact wavelength.

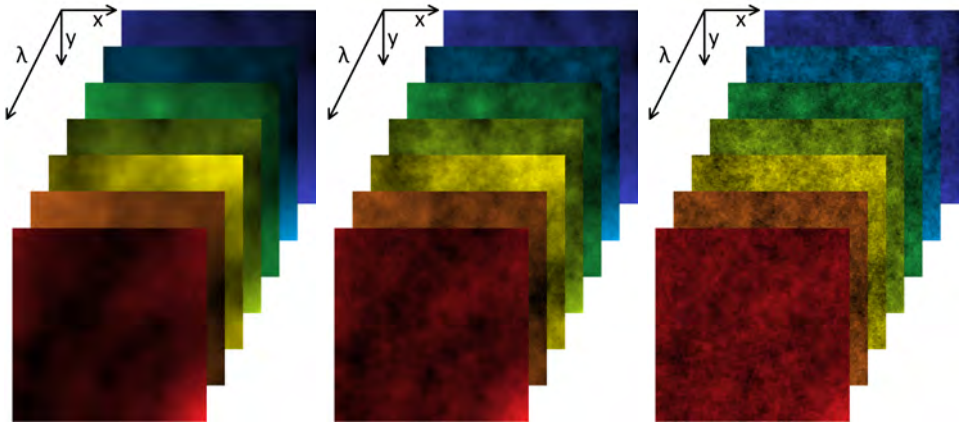

(a) Low complexity MSFI (b) Mid complexity MSFI (c) High complexity MSFI

Figure 4: The multi-spectral fractal images data cubes.

2.3 Visualization of multi-spectral images

There is a plethora of approaches regarding the multi-spectral and hyper-spectral image visualization and choosing the most appropriate one is not trivial, as the appropriate visualization can be of high importance for the consequent analysis tasks [34]. The existing visualization approaches can be categorized from the simplest band selection, to model-based approaches or approaches based on digital image processing techniques, and up to more recent methods using machine learning and deep learning paradigms [7].

Band selection consists of a mechanism of choosing three spectral bands from the spectral image and mapping them as the red, green and blue channels in the resulting color image. The selection can be performed manually by the user, as in software products such as ENVI [1] or automatically by unsupervised approaches based on the one-bit transform (1BT) [9], normalized

information (NI) [32], linear prediction (LP) or the minimum end member abundance co-variance [46]. Another set of approaches deploy the principal component analysis (PCA) for dimensionality reduction of the spectral image data. The straightforward way is to map the first three principal components to the R, G and B channels of the color image [50]. Other methods use PCA as part of a more complex approach: in [8] an interactive visualization technique based on PCA, followed by convex optimization is proposed; in [30] the color RGB image is obtained by fusing the spectral bands with saliency maps obtained before and after applying PCA; in [27], the spectral image is decomposed into two different layers (base and detail) through edge-preserving filtering and dimensionality reduction is performed using PCA applied on the base layer and a weighted averaging-based fusion on the detail layer, with the final result being a combination of the two layers. Another set of approaches are based on digital image processing techniques: [15] uses a multidimensional scaling, followed by detail enhancement using a Laplacian pyramid; [28] uses averaging in order to reduce the number of bands to 9, then a decolorization algorithm is applied on groups of three adjacent channels, thus producing the final RGB color image; [54] is based on t-distributed stochastic neighbor embedding (t-SNE) and bilateral filtering; [13] is also based on bilateral filtering, combined with high-dynamic range processing; [36] describes a pairwise-distances-analysis-driven visualization technique.

One approach we embrassed for the visualization of the generated synthetic multi-spectral images is based on a linear model of color formation proposed in [7]. In this approach, the resulting RGB triplet is obtain by integrating the product of the spectral reflectance curve of each pixel and the spectral sensitivity curve of a camera over the corresponding interval of wavelengths in the visible spectrum. Other linear methods for visualization exist: in [23] and [24], the RGB values are computed as projections of the hyperspectral pixel values on a particular vector basis like a stretched version of the CIE 1964 color matching functions, a constant-luma disc basis or an unwrapped cosine basis.

Another approach we embraced for visualization is the one based on artificial neural networks trained to learn the correspondence between spectral signatures and RGB triplets [7]. Spectral image visualization methods based on machine learning or deep learning usually rely on a pair of matched images, one spectral and one color. The latter one is either obtained through band selection from the spectral image or is independently captured by a different color image sensor. In remote sensing, the two images are registered in order to represent the same geographical area. Such approaches include constrained manifold learning [35], self-organizing maps [26], a moving least squares framework [34], a multi-channel pulse-coupled neural network [11] or

convolutional neural networks (CNNs) [10][48].

For each multi-spectral image, in Figures 5, 6 and 7, we show in (a) the color RGB image obtained by using the band-selection technique. The following wavelengths: 650, 550 and 450 nm were chosen for the R, G and B channels, respectively, in order to produce the color RGB rendering of the corresponding multi-spectral images. However, displaying a multi-spectral image poses the problem of reducing the potentially-large number of bands to just three color RGB channels in order for it to be rendered on a computer monitor, while ensuring that the displayed information is meaningful from the user point of view. In Figures 5, 6 and 7 (b) and (c) we depict the RGB color images obtained using the linear model and the artificial neural network approaches proposed in [7]. One can observe noticeable differences between the three types of visualization results (including the band selection approach). One reason is that the different visualization techniques tend to produce different results, as one can observe in [7]. Another reason is that the resulting multi-spectral pixel values in the synthetic fractal images have high variability due to the randomness in the generation mechanism and the statistical independence between bands, more than the variability of a natural spectral signature resulting in the acquisition process of a real scene. Last but not least, in all three cases the original information, which was more complex, was reduced to less information (the dimensionality reduction is from 7 spectral bands to only 3), so more than half of the information is lost in the process of rendering the color RGB composite image.

(a) BS RGB (b) Lin RGB (c) ANN RGB

Figure 5: The RGB color composite images of MSI in Figure 1.

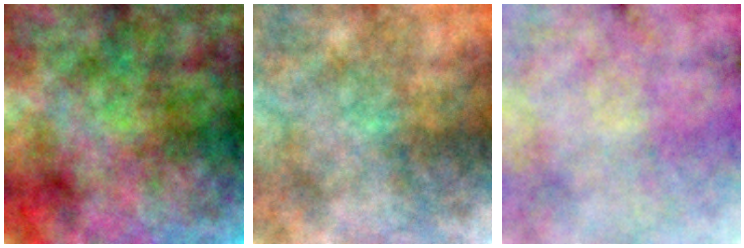

(a) BS RGB (b) Lin RGB (c) ANN RGB

Figure 6: The RGB color composite images of MSI in Figure 2.

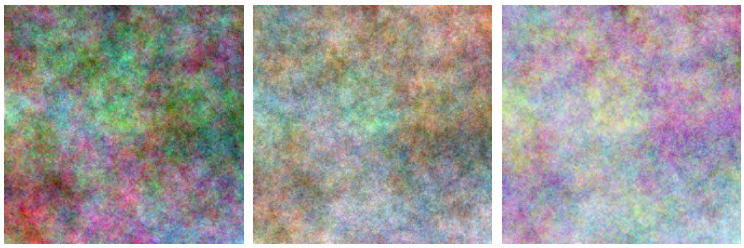

(a) BS RGB (b) Lin RGB (c) ANN RGB

Figure 7: The RGB color composite images of MSI in Figure 3.

2.4 Mathematical proof

Now for the generated synthetic fractal multi-spectral images the question is: are they fractal objects? More concretely, is the variance of the increments resulted in the generation process obeying the fractal conditions? In this section, the generation of multi-spectral fractal images with independent spectral bands is validated mathematically, before showing its possible usage in experiments. In [18] it is shown that the resulting color fractal images with 3 statistically independent color components obey the law of direct proportionality of the variance of the increments. We shall take the same approach for the multi-spectral fractal images with M independent bands.

For an object or signal X, having two spatial arguments and M-dimensional vector values (i.e. for the M spectral bands), the variance of the vectorial increments (considering an Euclidean distance between two samples of the signal X) is the following:

$$\sigma_i^2 = \overline{\left\{ \sqrt{\sum_{k=1}^{M} \left[X_k(t_1, t_2) - X_k(s_1, s_2) \right]^2} \right\}^2} \tag{5}$$

Raising the square root to the power of two in eq. (5) and taking into account that the quantities under the square root are positive, one gets the following expression:

$$\sigma_i^2 = \overline{\sum_{k=1}^{M} \left[X_k(t_1, t_2) - X_k(s_1, s_2)\right]^2} \tag{6}$$

Now the statistical operator can be distributed to all the M terms, regardless they are correlated or not:

$$\sigma_i^2 = \sum_{k=1}^{M} \overline{\left[X_k(t_1, t_2) - X_k(s_1, s_2)\right]^2} \tag{7}$$

By identifying each term, it represents the marginal variance of the signal X for each spectral band, respectively. They should be statistically independent and, each of them, obeying the fractal law in the generation process, assuming a Hurst coefficient identical for all spectra bands:

$$\sigma_i^2 \propto \left(\sum_{i=1}^{2} (t_i - s_i)^2\right)^H \tag{8}$$

Consequently, the variance of the vectorial increments of the X signal is directly proportional to:

$$\sigma_i^2 \propto M \left(\sum_{i=1}^{2} (t_i - s_i)^2\right)^H \propto \left(\sum_{i=1}^{2} (t_i - s_i)^2\right)^H \tag{9}$$

which proves that for a multi-spectral image with M statistically-independent spectral bands, the variance of the M-dimensional increments obeys the self-similarity statistical law in eq. (8), thus validating the generation of synthetic multi-spectral images with fractal properties. In conclusion, we analytically showed in eq. (9) that the multi-spectral fractal images with independent spectral bands are also obeying the fractal law, consequently they are fractal objects, enabling the estimation of their multi-spectral fractal dimension.

2.5 Fractal dimension estimation for multi-spectral images

We embraced the approach in [21], which allows extending the classical probabilistic box-counting from 3 color channels to theoretically any number of

spectral bands. In order to compute the $N(\delta)$ measure required for the fractal dimension estimation, one has to adapt the analysis boxes for the multi-spectral case. In Figure 8 we show the multi-spectral boxes of size $\delta = 3$ and $\delta = 5$ for the case of multi-spectral images with 2 spatial coordinates and $M = 7$ spectral bands.

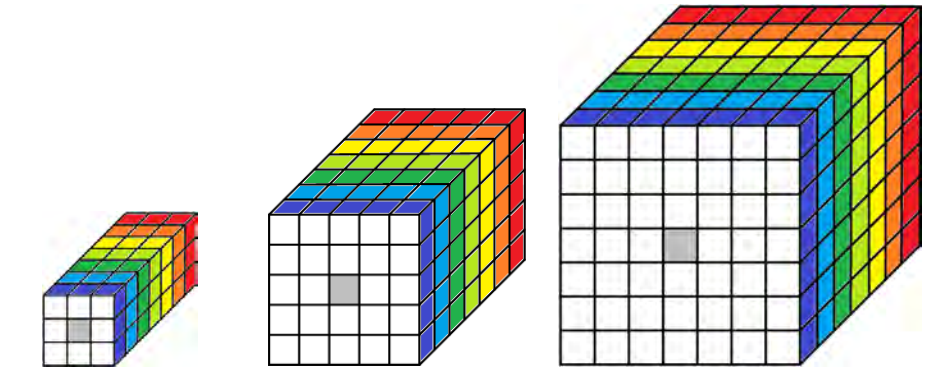

(a) $\underbrace{3 \times 3 \times \cdots \times 3}_{9 \text{ times}}$ (b) $\underbrace{5 \times 5 \times \cdots \times 5}_{9 \text{ times}}$ (c) $\underbrace{7 \times 7 \times \cdots \times 7}_{9 \text{ times}}$

Figure 8: The analysis boxes for size $\delta = 3$, $\delta = 5$ and $\delta = 7$.

In Figure 9 we depict, in blue, the vector value of one randomly-chosen reddish pixel in the multi-spectral image from Figure 4(b), illustrating, with light grey, the box of size δ around the pixel's spectral value. The box size is very often varied from 3 to 41 in steps of 2 (i.e. only the odd-size boxes for a simpler implementation). For a specific value of δ, in the estimation of the $N(\delta)$ measure, and for a spectral pixel vector value $S(\lambda)$, the upper and lower δ-parallel covers indicating the limits of the analysis boxes (hyper-cubes) are given by $S(\lambda) + \frac{\delta}{2}$ and $S(\lambda) - \frac{\delta}{2}$, respectively.

One question emerging from this experimental setup is about the pertinence of the embraced fractal model with respect to the generation of multi-spectral images with spectral pixel values corresponding to real spectra. Is the spectral pixel value in Figure 9 a valid spectral signature, which could represent a real remotely-sensed spectrum from a real scene on the surface of the Earth? To a certain extent, the answer is yes. Given that a reddish pixel was chosen from the lower-right corner of the multi-spectral image in Figure **??**(b), the shape of the spectral pixel value is pertinent, showing higher values corresponding to the interval corresponding to the red wavelengths. Also, given the relatively large distances between spectral bands (i.e. 50 nm), one can assume that the neighbor values in the spectral signature of the pixels are statistically-independent, which is the case in the embraced model. Evidently, for the synthesis of fractal higher-spectral resolution images (like

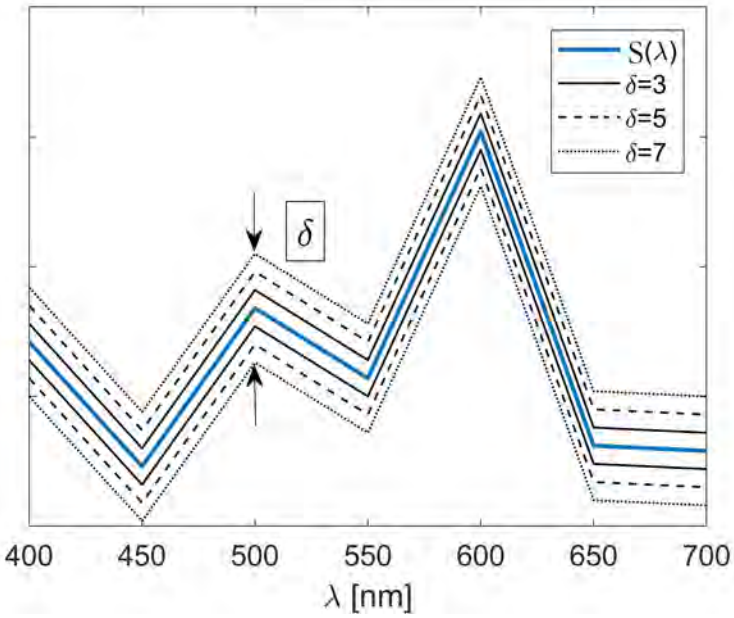

Figure 9: One pixel value (in blue) and the corresponding area between the δ-parallel covers (for $\delta = 3, 5, 7$).

hyper-spectral images), this assumption does not stand anymore.

3 Fine tuning the estimator

In order to experimentally test and validate the proposed approach, we considered the three generated multi-spectral fractal data cubes or images with 7 spectral bands in Figure 4, having a spatial resolution of 256×256 pixels, of varying fractal complexity (i.e. low, medium and high which translates into a Hurst coefficient of 0.9, 0.5 and 0.1 respectively). As we mentioned in the theoretical considertions, the fractal dimension of such a multi-spectral fractal image should be comprised between 2 (the complexity of a plane for a *uni* image or an image having the same color in every pixel) and 9 (the highest achievable for a 9 dimensional image, i.e. $2+7$, 2 spatial coordinates plus 7 spectral coordinates). For the three synthetic multi-spectral images, we ran the proposed probabilistic box-counting fractal dimension estimation adapted to the multi-spectral case. The maximum analysis window size δ_{max} was varied for all three images from 41 to 101 in steps of 10. However, the maximum analysis window was set to smaller values for the low and mid complexity images, as a maximum window of 31 proved to be very large, especially for the low complexity image. The threshold for the standard de-

viation σ_{th} was varied from 10^{-4} to 10^{-10} in steps of 10^{-1}. This standard deviation refers to the extent to which the regression line slope estimation approaches should agree on the $N(\delta)$ measure, which has a direct impact on the fractal dimension estimation. For the three multi-spectral images we obtained the numerical results presented in Tables 2, 3 and 4 for the low, mid and high complexity, respectively.

δ_{max} \ σ_{th}	10^{-4}	10^{-5}	10^{-6}	10^{-7}	10^{-8}	10^{-9}	10^{-10}
7	2.2727	2.2727	2.2727	2.2727	2.2727	2.2727	2.2727
11	2.4790	**2.7653**	**2.7653**	**2.7653**	**2.7653**	2.6934	2.6934
21	2.5873	2.5578	2.5411	2.5308	2.5268	2.5268	2.5257
31	2.5393	2.5134	2.5134	2.5134	2.5083	2.5083	2.4816
41	2.5233	2.5065	2.5013	2.4965	2.4755	2.4755	2.4733
51	2.5014	2.4893	2.4839	2.4604	2.4574	2.4394	2.4394
61	2.4903	2.4786	2.4533	2.4471	2.4443	2.4164	2.4080
71	2.4702	2.4625	2.4468	2.4439	2.4414	2.4320	2.4214
81	2.4693	2.4613	2.4539	2.4473	2.4302	2.4269	2.4269
91	2.4773	2.4606	2.4469	2.4391	2.4321	2.3607	2.3651
101	2.4695	2.4397	2.4165	2.3596	2.3587	2.3587	2.3579

Table 2: The estimated multi-spectral fractal dimension (MFD) of multi-spectral fractal image with low complexity ($H = 0.9$).

δ_{max} \ σ_{th}	10^{-4}	10^{-5}	10^{-6}	10^{-7}	10^{-8}	10^{-9}	10^{-10}
21	3.5975	3.8173	3.8173	3.9665	3.9665	3.9665	3.9665
31	4.1713	4.1713	4.2113	4.2113	**4.2229**	**4.2229**	**4.2229**
41	4.1952	4.2133	4.2133	4.2133	4.1150	4.1150	4.1150
51	4.1619	4.1619	4.1334	4.1157	3.9118	3.9118	3.9118
61	4.1040	4.1175	4.0941	3.9299	3.9299	3.6920	3.6920
71	4.0611	4.0737	4.0531	4.0342	3.5104	3.5104	3.5104
81	4.0154	4.0333	3.9957	3.9744	3.3457	3.3457	3.3287
91	3.9682	3.9682	3.9462	3.2035	3.1677	3.1677	3.1523
101	3.8944	3.9172	3.8935	3.0930	3.0742	3.0652	3.0572

Table 3: The estimated multi-spectral fractal dimension (MFD) of multi-spectral fractal image with mid complexity ($H = 0.5$).

For the lowest complexity image, the highest achievable fractal dimension is 2.7653 for $\delta_{max} = 11$ and for the standard deviation comprised between 10^{-5} and 10^{-8}. For the mid complexity image, the highest achievable fractal

δ_{max} \ σ_{th}	10^{-4}	10^{-5}	10^{-6}	10^{-7}	10^{-8}	10^{-9}	10^{-10}
41	0.7523	1.1958	4.5693	5.1281	5.1281	5.1281	5.1281
51	5.4481	5.8568	5.9662	5.9662	5.9662	5.9662	5.9662
61	5.7691	6.0965	6.4867	6.4867	6.4867	6.4867	6.4867
71	6.1941	6.5484	6.6172	6.6555	6.6555	6.6555	6.6555
81	6.5319	6.5319	6.5089	6.3486	6.3486	6.1297	6.1297
91	6.4054	6.4419	6.4574	6.4574	**6.6636**	**6.6636**	**6.6636**
101	6.3180	5.7551	5.2170	5.2170	5.0599	5.0599	5.0599

Table 4: The estimated multi-spectral fractal dimension (MFD) of multi-spectral fractal image with high complexity ($H = 0.1$).

dimension is 4.229 for $\delta_{max} = 31$ and for the standard deviation comprised between 10^{-8} and 10^{-10}. Important to mention the fact that when setting a threshold to such small values, the estimated fractal dimension is estimated based only on 3 points in the $N(\delta)$ measure. A more reliable estimation would be 4.2133 for $\delta_{max} = 41$ and for the standard deviation comprised between 10^{-5} and 10^{-7}. For the high complexity image, the highest achievable fractal dimension is 6.6636 for $\delta_{max} = 91$ and for the standard deviation comprised between 10^{-8} and 10^{-10}. Making the same observation as before, a more confident estimation would be 6.6555 for $\delta_{max} = 71$ and for the standard deviation comprised between 10^{-7} and 10^{-10}. As a general observation, the estimated fractal dimensions are indicating the correct ranking of the generated image complexity. In addition, as expected, the parameter δ_{max} has to be adapted to the complexity of the image, which in practical application of the fractal estimation approach leads to a paradoxical situation: the fractal dimension which is desired to be estimated, thus unknown, should be known in order to set the correct parameter values for the estimator. Another important observation is that, comparing the current obtained results to the one obtained for color fractal images in [21], the extra information due to the additional 4 spectral bands, compared to the color RGB case, leads to higher values of complexity.

In order to graphically observe the evolution of the estimated multi-spectral fractal dimension, we present the corresponding plots in Figures 10 12 and 14 (the evolution as a function of δ_{max}) and Figures 11 13 and 15 (the evolution as a function of σ_{th}), for the low, mid and high complexity, respectively, for the common interval of parameter values (δ_{max} from 41 to 101 and σ_{th} from 10^{-4} to 10^{-10}). As a general observation, for the low and mid complexity images, the tendency of the estimated multi-spectral fractal dimension is to decrease with the increase of the maximum analysis window

and the increase of precision for the agreement of regression lines estimators (decrease of the standard deviation). However, this behavior in observed outside the most pertinent interval of values for δ_{max}. A possible explanation for the low performance of the estimator for large values of the maximum analysis box size is the less statistically-significant data deployed in the regression line estimation as a consequence of the smaller effective image area for which the fractal analysis is performed (for $\delta_{max} = 101$ approximately 37% of the pixels of the generated images are disregarded). If the image spatial resolution (i.e. the image size) would allow, increasing the size of the maximum analysis box makes sense, given that the current estimator disregards the small boxes and allocates more weight to the larger boxes. Especially, for the high complexity fractal images, where the variations of the signals can be very important, thus the need to adapt the maximum analysis window. For the high complexity image, the variation of the analysis box size δ_{max} show that the mid range of values are the most pertinent for the estimation. For the appropriate values of δ_{max}, increasing the precision of the slope agreement in the regression line estimators (thus diminishing the standard deviation) is clearly improving the estimation, as the estimated multi-spectral dimension increases.

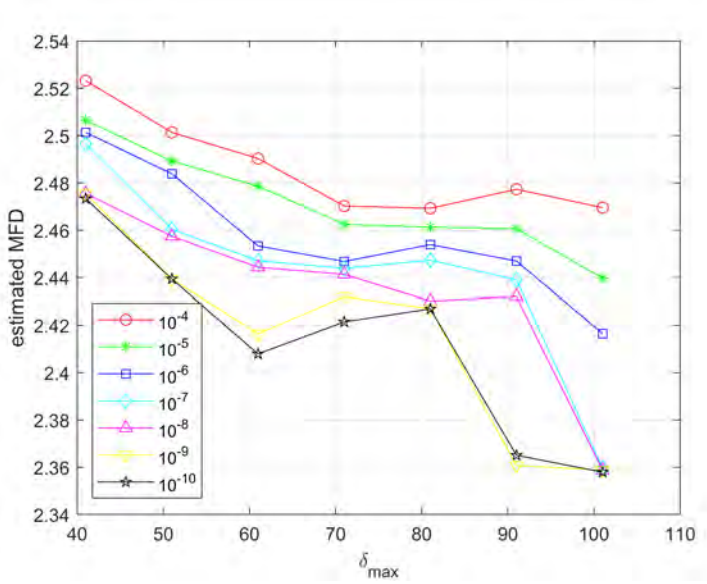

Figure 10: The estimated multi-spectral fractal dimension as a function of δ_{max} for the low complexity ($H = 0.9$) multi-spectral fractal image.

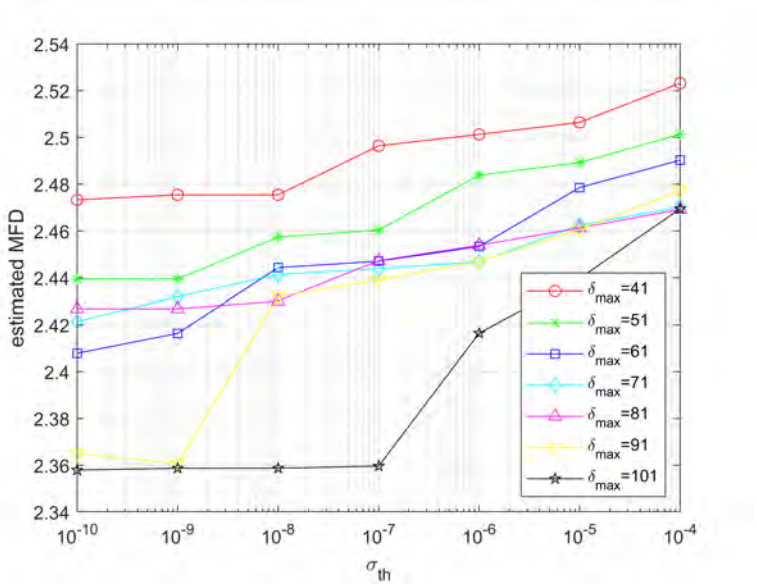

Figure 11: The estimated multi-spectral fractal dimension as a function of σ_{th} for the low complexity ($H = 0.9$) multi-spectral fractal image.

4 Experimental results

The multi-spectral images used in our experiments are two crops (left upper corner and right lower corner) of Pavia University hyper-spectral image, down sampled in the spectral domain to only 7 spectral bands. Pavia University data set is a 610 × 340 image, with a spectral resolution of $4nm$ and a spatial resolution of 1.3 meters. The image has 103 bands in the 430-860 nm range. The scene in the image contains a number of 9 materials according to the provided ground truth, both natural and man-made. We selected 7 spectral bands from the hyper-spectral data: 1, 14, 26, 39, 51, 64, 76, corresponding to the 430, 482, 530, 582, 630, 682 and 730 nm wavelengths. We cropped the left upper corner and the right lower corner of the image, so that the spatial resolution is 256 × 256 pixels, similar to the one of the synthetic fractal images used for validation (see Figures 16 and 17). The estimated multi-spectral fractal dimension of the 7 spectral bands Pavia University multi-spectral image crops is presented in Tables 5 and 6, for δ_{max} varied between 31 and 71 in steps of 10 and σ_{th} varied from 10^{-4} to 10^{-8} in steps of 10^{-1}, i.e. the settings for the most confident estimation results considering a parameter setting of the estimation tool for rather low to mid-complexity images, for the considered Pavia University multi-spectral images.

For the left upper corner crop of Pavia University image, the maximum

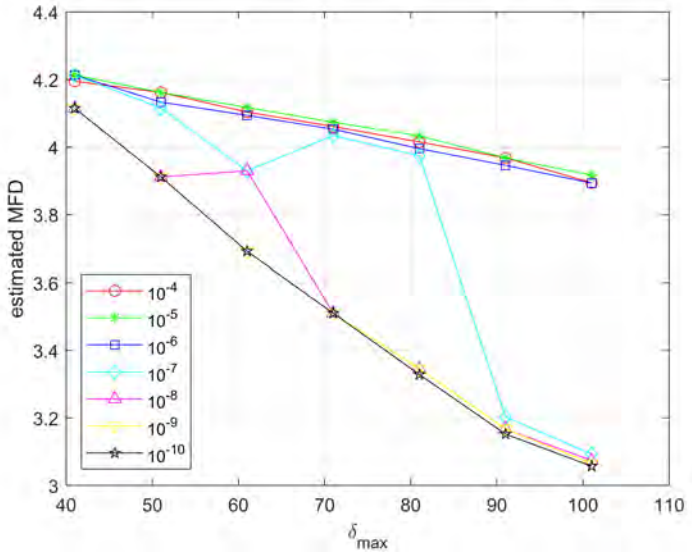

Figure 12: The estimated multi-spectral fractal dimension as a function of δ_{max} for the mid complexity ($H = 0.5$) multi-spectral fractal image.

estimated multi-spectral fractal dimension is 3.5072, while for the right lower corner crop is 3.0456. The relative difference in complexity is obvious due to the image content: the more complex image contains more colors and variations, with more objects present in the scene, while the less complex image contains less colors, less objects and a larger area of small signal variations. Consequently, the estimator clearly indicates the relative ranking of images as a function of their complexity. Both images, though, by their complexity are in the mid-low complexity range.

δ_{max} \ σ_{th}	10^{-4}	10^{-5}	10^{-6}	10^{-7}	10^{-8}
31	3.2891	3.3425	3.4251	3.4876	3.5405
41	3.4330	3.5144	3.4140	3.4140	3.4140
51	3.4891	**3.5072**	**3.5072**	3.2730	3.2730
61	3.3639	3.3863	3.3595	3.3595	3.0681
71	3.2634	3.2879	3.2879	2.4161	2.4161

Table 5: The estimated multi-spectral fractal dimension (MFD) of the Pavia University multi-spectral image (left upper corner).

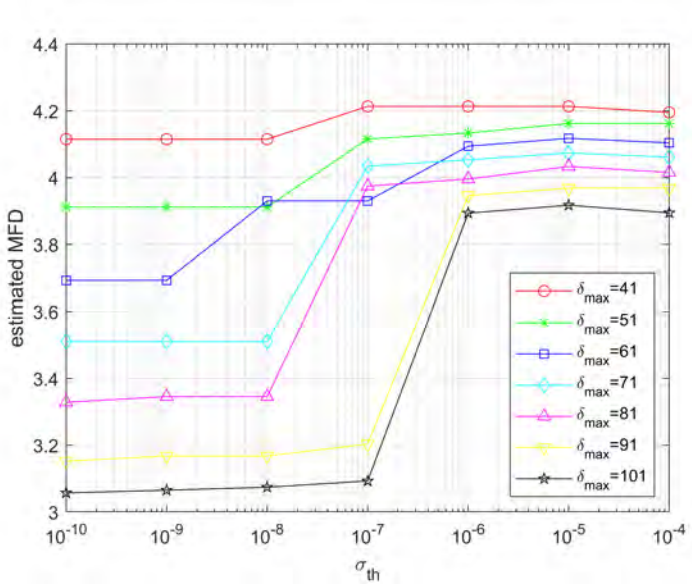

Figure 13: The estimated multi-spectral fractal dimension as a function of σ_{th} for the mid complexity ($H = 0.5$) multi-spectral fractal image.

5 Conclusions

We proposed both a generator and fractal dimension estimator for multi-spectral images. The generator is based on the midpoint displacement algorithm used for generating fractional Brownian motion and the estimator is based on the classical probabilistic box-counting approach. The model for the generated multi-spectral fractal images is proved mathematically and illustrated for the case of 7 statistically-independent spectral bands. The model can be extended theoretically to an arbitrary number of spectral bands, as long as the hypothesis of statistical independence between bands holds (which may not be the case for high spectral resolution images, like hyper-spectral images). For a qualitative evaluation, the resulting synthetic multi-spectral data sets were visualized as color RGB composites using three different approaches: the widely-used band selection, using a linear model for the color formation and deploying an artificial neural network which was previously trained to learn the correspondences between the multi-spectral pixel signatures and colors specified in the RGB color space. The estimator was adapted to work on 9-dimensional fractal objects and we estimated the multi-spectral fractal dimension of the generated synthetic multi-spectral fractal images. The estimation requires the setting of the values for the parameters δ_{max} and σ_{th}, as they should be adapted to the envisaged complexity range of

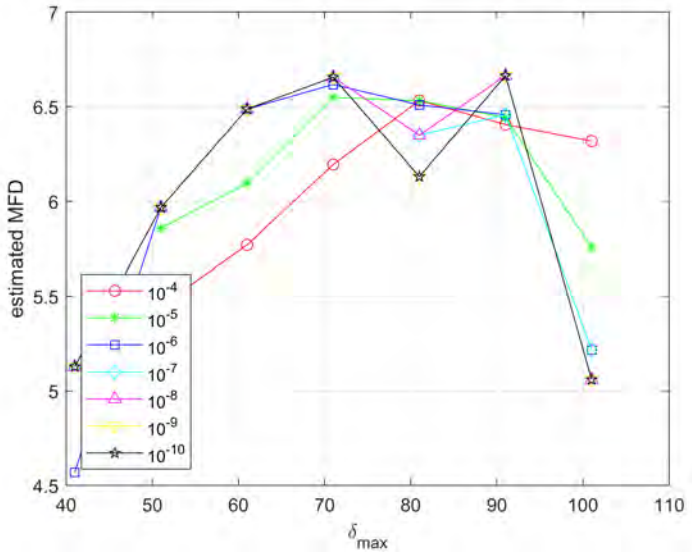

Figure 14: The estimated multi-spectral fractal dimension as a function of δ_{max} for the high complexity ($H = 0.1$) multi-spectral fractal image.

the images. We presented and interpreted the numerical results obtained in the process of fine-tuning the estimator. However, for the high complexity image, the desirable multi-spectral dimension of 8.3 is not yet achieved.

Furthermore, we used the proposed multi-spectral fractal dimension estimator for the fractal complexity assessment of real images. We chose for experiments the widely-known Pavia University hyper-spectral data set which was first down sampled in the spectral domain from 103 spectral bands to only 7 spectral bands, in order to fit to the spectral capabilities of the designed estimator; secondly, the image was cropped so that the spatial resolution of the resulting images to be identical to the one of the generated synthetic multi-spectral fractal images (256×256). The dynamic range was also scaled to the $[0 - 255]$ interval, in order to have the same variation of values on all 7 bands and in the same range as the spatial domain. The obtained results are in accordance with the perceived complexity of the two scenes. As future directions, the proposed multi-spectral fractal dimension estimator can be used to estimate the local or global complexity of multi-spectral images, for example in two types of applications—image classification and image segmentation—, where the multi-spectral fractal dimension can be used as a global or local feature, respectively, for multi-spectral texture characterization. The proposed model and estimator can be applied on remotely-sensed data, like the multi-spectral images from the Sentinel 2

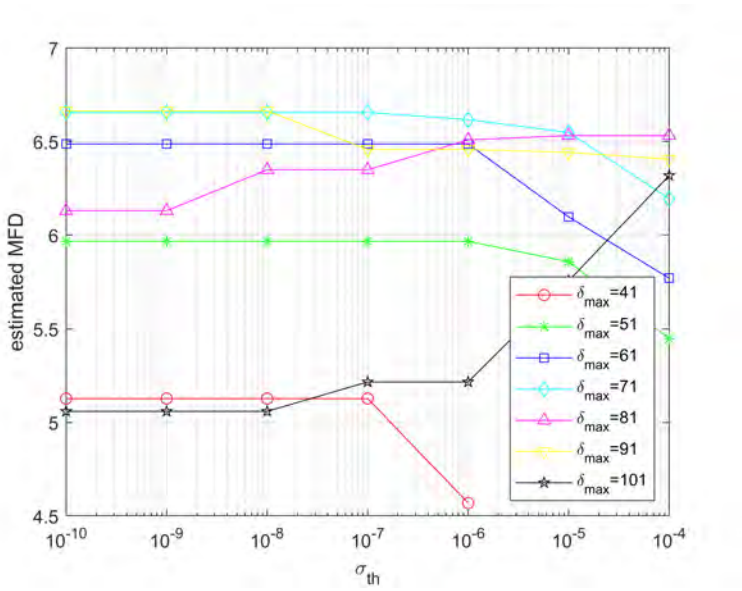

Figure 15: The estimated multi-spectral fractal dimension as a function of σ_{th} for the high complexity ($H = 0.1$) multi-spectral fractal image.

satellites of the Copernicus Earth Observation programme.

6 Acknowledgments

This work was funded from the AI4AGRI project entitled "Romanian Excellence Center on Artificial Intelligence on Earth Observation Data for Agriculture". The AI4AGRI project received funding from the European Union's Horizon Europe research and innovation programme under the grant agreement no. 101079136.

Funded by the European Union. Views and opinions expressed are however those of the author(s) only and do not necessarily reflect those of the European Union. Neither the European Union nor the granting authority can be held responsible for them.

References

[1] `https://www.harrisgeospatial.com/Software-Technology/ENVI/`.

[2] Isabel Cecilia Contreras Acosta, Mahdi Khodadadzadeh, Laura Tusa, Pedram Ghamisi, and Richard Gloaguen. A machine learning framework for drill-core mineral mapping using hyperspectral and high-resolution mineralogical data fusion. *IEEE Journal of Selected Topics in Applied Earth Observations and Remote Sensing*, 12(12):4829–4842, 2019.

[3] B. Aiazzi, L. Alparone, S. Baronti, A. Bulletti, and A. Garzelli. Robust estimation of image fractal dimension based on pyramidal decomposition.

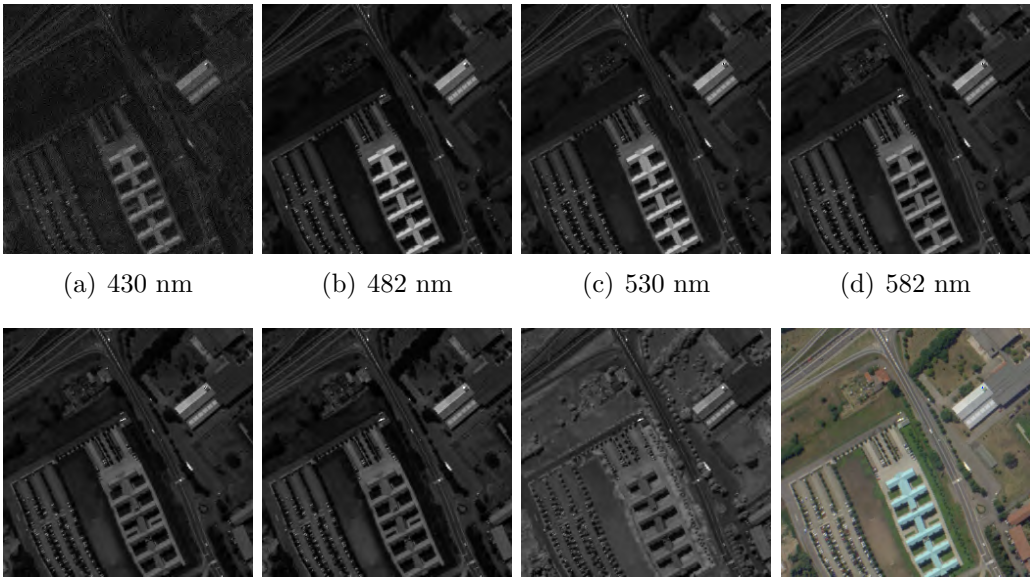

(a) 430 nm (b) 482 nm (c) 530 nm (d) 582 nm

(e) 602 nm (f) 640 nm (g) 730 nm (h) BS RGB

Figure 16: The 7 spectral bands of the Pavia University MSI and the correponding band-selection (10, 31, 46) color RGB image for the Pavia University hyperspectral data set (left upper corner).

In *6th IEEE International Conference on Electronic, Circuits ans Systems*, volume 1, pages 553–556, May 1999.

[4] C. Allain and M. Cloitre. Characterizing the lacunarity of random and deterministic fractal sets. *Physical review A*, 44(6):3552–3558, September 1991.

[5] O. Castillo and P. Melin. A new method for fuzzy estimation of the fractal dimension and its applications to time series analysis and pattern recognition. In *Fuzzy Information Processing Society, 2000. NAFIPS. 19th International Conference of the North American*, pages 451–455, Atlanta, July 2000. IEEE.

[6] W.S. Chen, S.Y. Yuan, H. Hsiao, and C.M. Hsieh. Algorithms to estimating fractal dimension of textured images. *IEEE International conferences on Acoustics, Speech and Signal Processing (ICASSP)*, 3:1541–1544, May 2001.

[7] Radu-Mihai Coliban, Maria Marincaş, Cosmin Hatfaludi, and Mihai Ivanovici. Linear and non-linear models for remotely-sensed hyperspectral image visualization. *Remote Sensing*, 12(15), 2020.

[8] Ming Cui, Anshuman Razdan, Jiuxiang Hu, and Peter Wonka. Interactive hyperspectral image visualization using convex optimization. *IEEE Transactions on Geoscience and Remote Sensing*, 47(6):1673–1684, 2009.

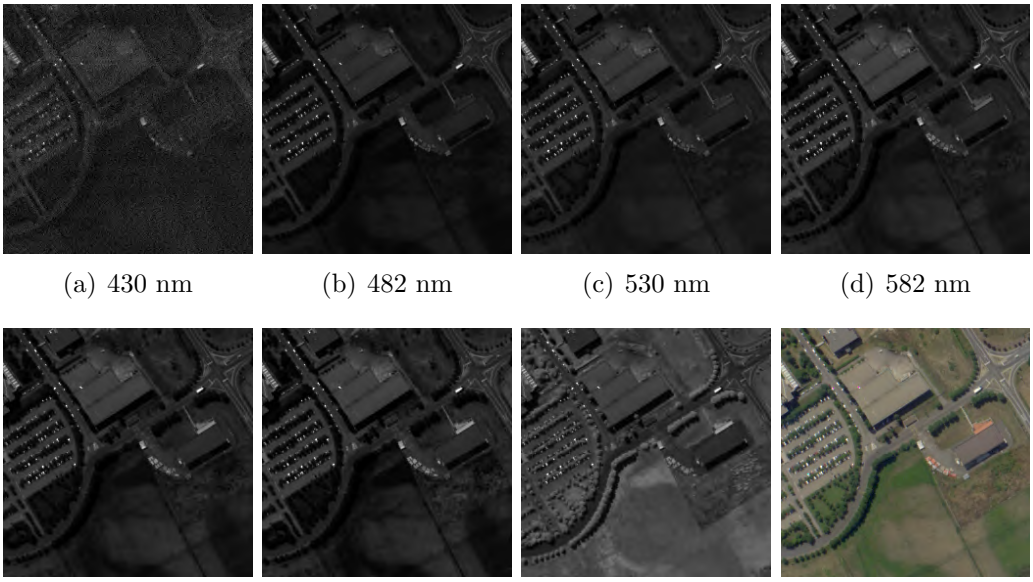

(a) 430 nm (b) 482 nm (c) 530 nm (d) 582 nm

(e) 630 nm (f) 682 nm (g) 730 nm (h) BS RGB

Figure 17: The 7 spectral bands of the Pavia University MSI and the correponding band-selection (10, 31, 46) color RGB image for the Pavia University hyperspectral data set (right lower corner).

[9] Begum Demir, Anil Celebi, and Sarp Erturk. A low-complexity approach for the color display of hyperspectral remote-sensing images using one-bit-transform-based band selection. *IEEE Transactions on Geoscience and Remote Sensing*, 47(1):97–105, 2008.

[10] Puhong Duan, Xudong Kang, and Shutao Li. Convolutional neural network for natural color visualization of hyperspectral images. In *IGARSS 2019-2019 IEEE International Geoscience and Remote Sensing Symposium*, pages 3372–3375. IEEE, 2019.

[11] Puhong Duan, Xudong Kang, Shutao Li, and Pedram Ghamisi. Multichannel pulse-coupled neural network-based hyperspectral image visualization. *IEEE Transactions on Geoscience and Remote Sensing*, 58(4):2444–2456, 2019.

[12] Ines Dumke, Stein M Nornes, Autun Purser, Yann Marcon, Martin Ludvigsen, Steinar L Ellefmo, Geir Johnsen, and Fredrik Søreide. First hyperspectral imaging survey of the deep seafloor: High-resolution mapping of manganese nodules. *Remote Sensing of Environment*, 209:19–30, 2018.

[13] Sarp Ertürk, Seçil Süer, and Hatice Koç. A high-dynamic-range-based approach for the display of hyperspectral images. *IEEE Geoscience and Remote Sensing Letters*, 11(11):2001–2004, 2014.

δ_{max} \ σ_{th}	10^{-4}	10^{-5}	10^{-6}	10^{-7}	10^{-8}
11	0.9443	1.4164	1.4164	1.4164	1.7307
21	2.7358	2.9679	2.9679	3.0386	3.0386
31	3.0320	3.0320	**3.0456**	**3.0456**	2.9699
41	2.9221	2.9221	2.7059	2.6599	2.6599
51	2.8264	2.8264	2.8324	2.5104	2.5464

Table 6: The estimated multi-spectral fractal dimension (MFD) of the Pavia University multi-spectral image (right lower corner).

[14] K. Falconer. *Fractal Geometry, mathematical foundations and applications.* John Wiley and Sons, 1990.

[15] Jialu Fang and Yuntao Qian. Local detail enhanced hyperspectral image visualization. In *2015 IEEE International Geoscience and Remote Sensing Symposium (IGARSS)*, pages 1092–1095. IEEE, 2015.

[16] Geoffrey A Fricker, Jonathan D Ventura, Jeffrey A Wolf, Malcolm P North, Frank W Davis, and Janet Franklin. A convolutional neural network classifier identifies tree species in mixed-conifer forest from hyperspectral imagery. *Remote Sensing*, 11(19):2326, 2019.

[17] F. Hausdorff. Dimension und äußeres maß. *Mathematische Annalen*, 79(1-2):157–179, March 1918.

[18] M. Ivanovici and N. Richard. Fractal dimension of color fractal images. *IEEE Transactions on Image Processing*, 20(1):227–235, January 2011.

[19] M. Ivanovici and N. Richard. Entropy versus fractal complexity for computer-generated color fractal images. In *4th CIE Expert Symposium on Colour and Visual Appearance*, Prague, 2016.

[20] M. Ivanovici, N. Richard, and D. Paulus. Color image segmentation. In C. Fernandez-Maloigne, editor, *Advanced Color Image Processing and Analysis*, chapter 8, pages 219–277. Springer, New York, 2013.

[21] Mihai Ivanovici. Fractal dimension of color fractal images with correlated color components. *IEEE Transactions on Image Processing*, 29:8069–8082, 2020.

[22] Mihai Ivanovici. A fractal dimension estimator for multispectral images. In *2022 12th Workshop on Hyperspectral Imaging and Signal Processing: Evolution in Remote Sensing (WHISPERS)*, pages 1–4, 2022.

[23] Nathaniel P Jacobson and Maya R Gupta. Design goals and solutions for display of hyperspectral images. *IEEE Transactions on Geoscience and Remote Sensing*, 43(11):2684–2692, 2005.

[24] Nathaniel P Jacobson, Maya R Gupta, and Jeffrey B Cole. Linear fusion of image sets for display. *IEEE Transactions on Geoscience and Remote Sensing*, 45(10):3277–3288, 2007.

[25] S. Jansson. *Evaluation of methods for estimating fractal properties of intensity images*. PhD thesis, Umea University, Sweden, October 2006.

[26] Johannes Jordan and Elli Angelopoulou. Hyperspectral image visualization with a 3-d self-organizing map. In *2013 5th Workshop on Hyperspectral Image and Signal Processing: Evolution in Remote Sensing (WHISPERS)*, pages 1–4. IEEE, 2013.

[27] Xudong Kang, Puhong Duan, and Shutao Li. Hyperspectral image visualization with edge-preserving filtering and principal component analysis. *Information Fusion*, 57:130–143, 2020.

[28] Xudong Kang, Puhong Duan, Shutao Li, and Jón Atli Benediktsson. Decolorization-based hyperspectral image visualization. *IEEE Transactions on Geoscience and Remote Sensing*, 56(8):4346–4360, 2018.

[29] J.M. Keller and S. Chen. Texture description and segmentation through fractal geometry. *Computer Vision, Graphics and Image processing*, 45:150–166, 1989.

[30] Haris Ahmad Khan, Muhammad Murtaza Khan, Khurram Khurshid, and Jocelyn Chanussot. Saliency based visualization of hyper-spectral images. In *2015 IEEE International Geoscience and Remote Sensing Symposium (IGARSS)*, pages 1096–1099. IEEE, 2015.

[31] W. Kinsner. A unified approach to fractal dimensions. In *4th IEEE International Conference on Cognitive Informatics*, pages 58–72, July 2005.

[32] Steven Le Moan, Alamin Mansouri, Yvon Voisin, and Jon Y Hardeberg. A constrained band selection method based on information measures for spectral image color visualization. *IEEE Transactions on Geoscience and Remote Sensing*, 49(12):5104–5115, 2011.

[33] W.L. Lee, Y.C. Chen, and K.S. Hsieh. Ultrasonic liver tissues classification by fractal feature vector based on m-band wavelet transform. *IEEE Transactions on Medical Imaging*, 22:382–392, 2003.

[34] Danping Liao, Siyu Chen, and Yuntao Qian. Visualization of hyperspectral images using moving least squares. In *2018 24th International Conference on Pattern Recognition (ICPR)*, pages 2851–2856. IEEE, 2018.

[35] Danping Liao, Yuntao Qian, and Yuan Yan Tang. Constrained manifold learning for hyperspectral imagery visualization. *IEEE Journal of Selected Topics in Applied Earth Observations and Remote Sensing*, 11(4):1213–1226, 2018.

[36] Yi Long, Heng-Chao Li, Turgay Celik, Nathan Longbotham, and William J Emery. Pairwise-distance-analysis-driven dimensionality reduction model with double mappings for hyperspectral image visualization. *Remote Sensing*, 7(6):7785–7808, 2015.

[37] B.B. Mandelbrot. *The Fractal Geometry of Nature*. W.H. Freeman and Co, New-York, 1982.

[38] A.G. Manousaki, A.G. Manios, E.I. Tsompanaki, and A.D. Tosca. Use of color texture in determining the nature of melanocytic skin lesions - a qualitative and quantitative approach. *Computers in Biology and Medicine*, 36:416–427, 2006.

[39] P. Maragos and F.K. Sun. Measuring the fractal dimension of signals: morphological covers and iterative optimization. *IEEE Transactions on signal Processing*, 41(1):108–121, Janvier 1993.

[40] S.R. Nayak, J. Mishra, and G. Palai. An extended dbc approach by using maximum euclidian distance for fractal dimension of color images. *Optik*, 166:110 – 115, 2018.

[41] W. Pedrycz and A. Bargiela. Fuzzy fractal dimensions and fuzzy modeling. *Information Sciences*, 153:199–216, 2003.

[42] H.O. Peitgen and D. Saupe. *The sciences of fractal images*. Springer Verlag, 1988.

[43] Rami Piiroinen, Janne Heiskanen, Eduardo Maeda, Arto Viinikka, and Petri Pellikka. Classification of tree species in a diverse african agroforestry landscape using imaging spectroscopy and laser scanning. *Remote Sensing*, 9(9):875, 2017.

[44] S Reshma and S Veni. Comparative analysis of classification techniques for crop classification using airborne hyperspectral data. In *2017 International Conference on Wireless Communications, Signal Processing and Networking (WiSPNET)*, pages 2272–2276. IEEE, 2017.

[45] I.H. Shahrezaei and H. Kim. Fractal analysis and texture classification of high-frequency multiplicative noise in sar sea-ice images based on a transform-domain image decomposition method. *IEEE Access*, 8:40198–40223, 2020.

[46] Hongjun Su, Qian Du, and Peijun Du. Hyperspectral imagery visualization using band selection. In *2012 4th Workshop on Hyperspectral Image and Signal Processing: Evolution in Remote Sensing (WHISPERS)*, pages 1–4. IEEE, 2012.

[47] W. Sun, G. Xu, P. Gong, and S. Liang. Fractal analysis of remotely sensed images: a review of methods and applications. *International Journal of Remote Sensing*, 27(22):4963–4990, November 2006.

[48] Rongxin Tang, Hualin Liu, Jingbo Wei, and Wenchao Tang. Supervised learning with convolutional neural networks for hyperspectral visualization. *Remote Sensing Letters*, 11(4):363–372, 2020.

[49] Mustafa Teke, Hüsne Seda Deveci, Onur Haliloğlu, Sevgi Zübeyde Gürbüz, and Ufuk Sakarya. A short survey of hyperspectral remote sensing applications in agriculture. In *2013 6th International Conference on Recent Advances in Space Technologies (RAST)*, pages 171–176. IEEE, 2013.

[50] J Scott Tyo, Athanasios Konsolakis, David I Diersen, and Richard Christopher Olsen. Principal-components-based display strategy for spectral imagery. *IEEE transactions on geoscience and remote sensing*, 41(3):708–718, 2003.

[51] R. Voss. Random fractals : characterization and measurement. *Scaling phenomena in disordered systems*, 10(1):51–61, 1986.

[52] W. Wang, W. Wang, and Z. Hu. Retinal vessel segmentation approach based on corrected morphological transformation and fractal dimension. *IET Image Processing*, 13(13):2538–2547, 2019.

[53] L. Wu, X. Liu, Q. Qin, B. Zhao, Y. Ma, M. Liu, and T. Jiang. Scaling correction of remotely sensed leaf area index for farmland landscape pattern with multitype spatial heterogeneities using fractal dimension and contextural parameters. *IEEE Journal of Selected Topics in Applied Earth Observations and Remote Sensing*, 11(5):1472–1481, 2018.

[54] Biyin Zhang and Xin Yu. Hyperspectral image visualization using t-distributed stochastic neighbor embedding. In Jianguo Liu and Hong Sun, editors, *MIPPR 2015: Remote Sensing Image Processing, Geographic Information Systems, and Other Applications*, volume 9815, pages 14 – 21. International Society for Optics and Photonics, SPIE, 2015.

[55] X. Zhao and X.Y. Wang. An approach to compute fractal dimension of color images. *Fractals*, 25, 2017.